Journal of Materials Science: Materials in Electronics (2020) 31:3387–3396
https://doi.org/10.1007/s10854-020-02887-w

Effect of CdO ratios on the structural and optical properties of CdO–TiO_2 nanocomposite thin films

K. Sahbeni[1,2] · M. Jlassi[3,4] · S. Khamlich[5] · M. Kandyla[6] · M. Kompitsas[6] · W. Dimassi[1]

Received: 29 September 2019 / Accepted: 7 January 2020 / Published online: 18 January 2020

Abstract

Nanocomposite CdO–TiO_2 thin films have been successfully synthesized via sol–gel and spin coating techniques. The physical properties of the prepared thin films were studied by varying the Cd:Ti ratio (0, 25, 50, 75, and 100%). The structural characterization has been performed by X-ray diffraction (XRD), Raman spectroscopy, and scanning electron microscopy (SEM). Optical transmission and reflectivity of the obtained films have been studied by UV–Vis-NIR spectroscopy. The obtained results showed that the amount of Cd into the TiO_2 matrix can significantly affect the properties of TiO_2 thin films; the XRD analysis revealed the appearance of new diffraction planes by increasing the of Cd:Ti ratios, a fact that was also confirmed by the Raman spectra. Effects of incorporated Cd amounts on the crystal phase, crystallite size, surface morphology were investigated. The results showed that most of Cd^{2+} substituted Ti^{4+} in the crystal lattice of TiO_2 and led to the appearance of the $CdTiO_3$ phase for thin films at a relatively low temperature, which inhibited the growth of crystallite size and suppressed the transformation from anatase to rutile of TiO_2 at 450 °C. Moreover, formation of different binary and ternary nanocomposite films are justified by varying the Cd:Ti ratios. The optical analysis revealed a high transparency in the visible region, strongly affected by the different Cd:Ti ratios. Incorporated CdO initially increased the bandgap for low values of the Cd:Ti ratio, followed by a bandgap decrease for the highest one.

1 Introduction

A nanocomposite film consists of at least two phases, a bulk matrix and a nanodimensional phase(s), or a nanocrystalline phase with another nanocrystalline phase [1]. Recently, nanocomposite thin films attracted significant attention, due to their improved mechanical, electrical, optical, chemical, magnetic, and electronic properties [2–8]. Furthermore, due to these unique physicochemical properties, nanocomposite thin films are currently used for different technological applications, for photocatalysis [9–11], solar cells [12], removal of acid orange from wastewater [13], antibacterial treatment [14], in ferroelectricity [15–17], and chemo-resistive hydrogen sensing [18], and more.

A nanocomposite thin film can generally be obtained by a binary combination of semiconductors such as ZnO–CdO [11, 19], TiO_2–CuO [20], ZnO–TiO_2 [21, 22], CdO–NiO [14], TiO_2–SiO_2 [12], and TiO_2–CdO [23–25]. The most promising techniques for preparation of such nanocomposite thin films are Pulsed Laser Deposition [26] and sol–gel, spin coating methods [10, 13, 24, 27].

The present investigation deals with the TiO_2–CdO nanocomposites and their properties. CdO was selected because

✉ K. Sahbeni
sahbani_kaouther@hotmail.fr

1 Laboratoire Des Nanomatériaux Et Des Systèmes Pour Les Energies Renouvelables, Centre de Recherche Et Des Technologies de L'Energie, Technopole de Borj-Cédria, BP 95, 2050 Hammam-Lif, Tunisie

2 Faculté Des Sciences de Bizerte, 7021 Jarzouna, Tunisie

3 Ecole Supérieure Des Sciences et Technologies du Design, Université de La Manouba, P5, Den Den, Tunisie

4 Laboratoire de Semi-conducteurs, Nano-structure et Technologie Avancée, Centre de Recherche et des Technologies de l'Energie, Technopole de Borj-Cédria, BP 95, 2050 Hammam-Lif, Tunisie

5 Nanoenergy for Sustainable Development in Africa (NESDAF),Material Research Department, iThemba LABS-National Research Foundation, 722, Somerset West, Cape Town 7129, South Africa

6 Theoretical and Physical Chemistry Institute, National Hellenic Research Foundation, 48Vasileos Konstantinou Ave, 11635 Athens, Greece

of its high electrical conductivity which results from oxygen vacancies and/or Cd interstitial atoms and are related to the growth process. In addition, CdO thin films are characterized by their high optical transmission in the visible spectral range [14]. Cadmium itself is a rather cost-effective material with broad availability [9]. For all above reasons, CdO has found useful applications.

Titanium oxide (TiO_2), on the other hand, is an n-type semiconducting ceramic material, and has been widely used in the nanocomposite thin film industry. In recent years, TiO_2 attracted attention among researchers, due to the following properties: it has wide bandgap E_g, is environmental friendly, and is cost-effective for applications. TiO_2 is known for its interesting properties (e.g., optical, physical, and electronic). Among the three natural crystallographic phases, anatase is the metastable phase, while rutile is thermodynamically the most stable phase [28, 29]. Anatase-to-rutile phase conversion is a reversible process in which breaking and re-arranging of bonds occur [30]. Around 600–700 °C, this conversion is irreversible [24–32]. Transformation of the anatase-to-rutile phase in TiO_2 nanocomposites could be also obtained by mixing TiO_2 and CdO with different ratios at 700 °C, compared to pure TiO_2 anatase phase [33].

Generally, nanocomposite thin film-based TiO_2–CdO are not widely investigated in the literature. Furthermore, the combination of TiO_2 and CdO revealed the spinal phase $CdTiO_3$ which has been extensively studied [34–36], as well as its reversible phase transformation from rhombohedral to orthorhombic structure at around 1000 °C [35]. However, only few reported works focused their investigation to the ilmenite-type rhombohedral structure of $CdTiO_3$, for thin films, at relatively low temperatures [23, 34, 35].

In this experiment, TiO_2–CdO nanocomposite thin films were prepared by a sol–gel method, containing a rutile phase and orthorhombic $CdTiO_3$ structure. They were synthesized with different Cd:Ti mass ratios and their effect on the structural, morphological, and optical properties of the obtained nanocomposite thin film was investigated.

2 Experimental details

Sol–gel-derived TiO_2–CdO thin films were prepared by mixing CdO into TiO_2 sols in a particular ratio. The precursor solutions of TiO_2 and CdO are prepared separately by the sol–gel method. To obtain the solutions, the precursor cadmium acetate dehydrate [Cd $(CH_3COO)_2$ $2H_2O$] (98%, Sigma Aldrich) and titanium (IV) isopropoxide ($C_{12}H_{28}O_4Ti$) were separately dissolved in a mixture of 2-methoxyethanol ($C_3H_8O_2$) (99.8%, Sigma Aldrich) and monoethanolamine (MEA). The concentration of the TiO_2 and CdO was fixed at 0.5 M. The resultant solution of TiO_2 was stirred at 80 °C for 1 h, while the solution of CdO was stirred for 2 h at 80 °C to yield clear and homogeneous solutions. The as-prepared solutions were aged for 24 h. Thereafter, the prepared CdO solution was added to the TiO_2 sol until the Cd:Ti ratio was adjusted (pure CdO and TiO_2, $Ti_{0.75}+Cd_{0.25}$ noted as TC25, $Ti_{0.5}+Cd_{0.5}$ noted as TC50, and $Ti_{0.25}+Cd_{0.75}$ noted as TC75). All mixed final sols were stirred and deposition was performed using the spin coating method on a glass substrate at a speed of 3000 rpm for 30 s. The as-deposited films were pre-heated at 300 °C at 10 min. The coating procedure was repeated four times with the same conditions. The films were annealed for one hour at 450 °C under atmospheric air.

Phase identification of the mixed oxide samples was carried out by X-ray diffraction (XRD). The diffractometer was operated at 40 kV, 40 mA, and the 2θ values in the range of 20–80°. The structural characteristics of the films were also investigated by a Raman spectroscopy using the 448 nm irradiation. The morphological properties were determined by a Scanning Electron Microscope (SEM). Finally, the optical reflectance and transmittance spectra were recorded with a Perkin Elmer UV–Vis-NIR Lambda 19 spectrophotometer in the range of 250–1200 nm. All measurements were carried out at room temperature.

3 Results and discussion

3.1 Structural analysis by X-ray diffraction (XRD) and Raman spectroscopy

Figure 1 shows the XRD patterns of TiO_2, CdO and three nanocomposite films containing different amounts of CdO. The TiO_2 pattern exhibits prominent diffraction peaks attributed to the tetragonal anatase phase, located at $2\theta = 25.32^{o}$ and 48.04° which are assigned to (101) and (200) plane reflections, respectively (JCPDS File Number 01–089-4921).

The diffractogram corresponding to TC25 samples indicates that Cd was incorporated into the TiO_2 matrix. For this low Cd:Ti ratio, various new peaks was attributed to the spinal $CdTiO_3$ and rutile phase of TiO_2 appear at 450 °C. Indeed, a strong decrease in the lines intensity corresponding to the anatase phase was observed, accompanied by the appearance of the rutile phase of TiO_2. These peaks of rutile phase of TiO_2 were detected at $2\theta = 27.45°$ and 36.08° and assigned to (110) and (101) planes, respectively (JCPDS Card No. 00–034-0180).

The increase of the Cd amount in the TiO_2 matrix (i.e., Cd:Ti ≥ 50%) leads to a total disappearance of the anatase phase, whereas that of rutile persists. This observation suggested that a gradual anatase-to-rutile transformation occurs by the addition of Cd in the TiO_2 matrix thin films. Several works from the literature have shown that the parameters that affect this type of phase transformation are temperature

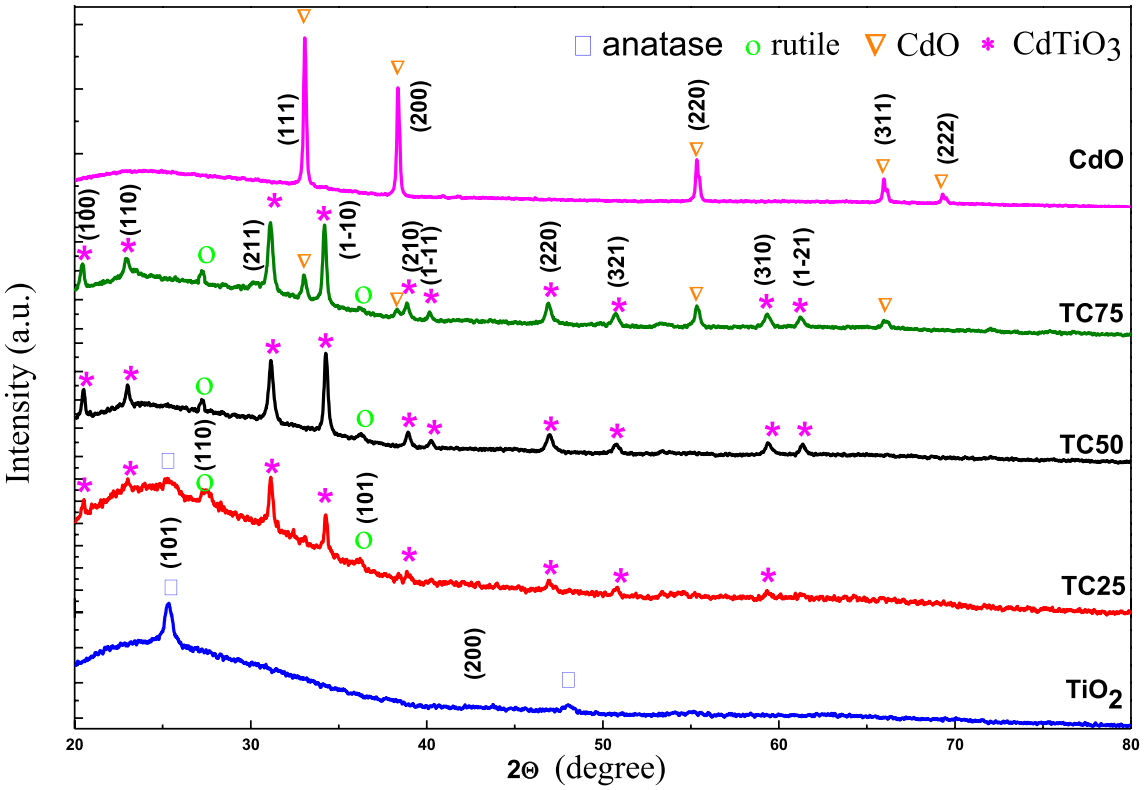

Fig. 1 XRD spectra of TiO_2, CdO and nanocomposite thin films with different Cd:Ti ratios on glass

[31, 32] and pressure [37]. In this context, the current work indicated that the incorporation of Cd into the TiO_2 matrix introduces another parameter relevant for this phase transformation. In fact, the formation of the rutile phase in doped samples can be explained assuming that Cd^{2+} ions are substitutionally incorporated into the lattice of the anatase TiO_2, promoting an increase of oxygen vacancies, similar to that reported by others [38, 39]. This increase presumably reduces the strain energy that must be overcome before a rearrangement of the structure can occur [38, 39]. Furthermore, the change of oxygen vacancies affects the second Ti_nO_{2n-1} variation Magnéli-type precipitated variation. The association of this last phase with Cd^{2+} can cause an increase in the rate of transformation which could provide nucleation centers of rutile [38]. It is clear that only the rutile phase exists, by increasing the Cd:Ti ratio; this confirms that this phase is more stable than that of anatase [28].

The $CdTiO_3$ spinal phase was detected for TC25, TC50, and TC75 spectra at $2\theta = 20.4°$, 22.9°, 34.2°, 38.9°, 40.2°, 47.9°, 50.7°, 53.3°, 59.3°, 61.3°, and 66.1° assigned to (100), (110), (110), (210), (111), (220), (321), (310) and (121) planes, respectively (according to JCPDS Card No. 01–085-0452). A notable intensity increase of $CdTiO_3$ peaks was observed with the increase of Cd:Ti ratio incorporated into TiO_2 matrix. In fact, the intensity of (110) which is the preferential direction of the $CdTiO_3$ attributed to the rhombohedral structure, increased with the increase in Cd content indicating good crystallinity. The rhombohedral structure of $CdTiO_3$ is observed for this work at 450 °C for 1 h annealing at atmospheric pressure and for thin films with an improved structure compared to the results given in the literature [27]. Dhivya et al. showed that $CdTiO_3$ crystallizes in the ilmenite rhombohedral phase when it is calcined above 800 °C [35], and Bersani mentioned that the usual preparation of $CdTiO_3$ takes place at high temperatures by heating the mixed solutions of CdO and TiO_2 at around 1000 °C in order to obtain the ilmenite phase. Heating time ranged from 24 to 34 h at atmospheric pressure which could be reduced to 60 min at 1.5 GPa [33, 40]. In the ilmenite structure, the TiO_6 octahedra are edge shared with the Cd^{2+} ion possessing a six-fold coordination [41]. Therefore, the incorporation of Cd into TiO_2 matrix is a major parameter, in addition to the temperature and pressure, causing structural modifications thin films, including both phase transformation (anatase to rutile) and causing the appearance of the $CdTiO_3$ ilmenite rhombohedral phase at 450 °C.

In the XRD spectrum corresponding to the highest Cd:Ti ratio, some additional reflection peaks appeared at $2\theta = 33°$, 38.4°, 55.3°, and 66° which were attributed to (110), (200), (220), and (311) planes, respectively, of the

CdO monteponite structure, according to JCPDS Card No. 01–075-0592, and indicating cubic structure.

From the full width at half maximum of the Bragg peaks, the average crystallite size of the samples with different compositions was calculated using Debye Scherrer's formula [26]:

$$D = \frac{k\lambda}{\beta \cos\theta} \quad (1)$$

where k is a shape factor of the particle (0.9), λ is the source wavelength 1.5404 Å, 2θ is the peak position, and $\beta_{1/2}$ is the full width at half maximum of the Bragg peak.

The crystallite sizes of all samples with anatase, rutile, CdO, and $CdTiO_3$ phases are summarized in Table 1, showing differences in particle sizes. For the TiO_2 anatase phase, we noticed a decrease in the crystallite size by adding CdO; the smaller crystallite size was attributed to a greater lattice distortion of the sample, caused by the larger incorporated amount of CdO. This could enhance the concentration of lattice defects and thus precipitate carrier recombination [42, 43]

These structural changes are due to differences in the ionic radii between Cd as the impurity ion and Ti as the host [44]. It is consistent with the Vegard's law [44], which states that, if the ionic radius of a dopant atom is larger than the ionic radius of the host, it leads to an increase in crystallinity. In the present study, the nanoparticle Cd^{2+} ion has a larger substituting radius (1.07 Å) than the smaller ionic radius of the host Ti^{4+} ion (0.68 Å), and the increased tendency for the agglomeration may lead to increased crystallite sizes for $CdTiO_3$ and rutile phases. However, the decrease of crystallite size observed in the $CdTiO_3$ and rutile phases

Table 1 Crystallite size (nm) of the anatase, rutile, $CdTiO_3$, and CdO phases, contained in prepared TiO_2, CdO, and nanocomposites thin films with different Cd:Ti ratios estimated from XRD spectrum

	TiO_2	25TC	50TC	75TC	CdO
TiO_2 Anatase (nm)	27	10	–	–	–
TiO_2 Rutile (nm)	–	20	34	23	–
$CdTiO_3$ (nm)	–	49	82	45	–
CdO (nm)	–	–	–	49	70

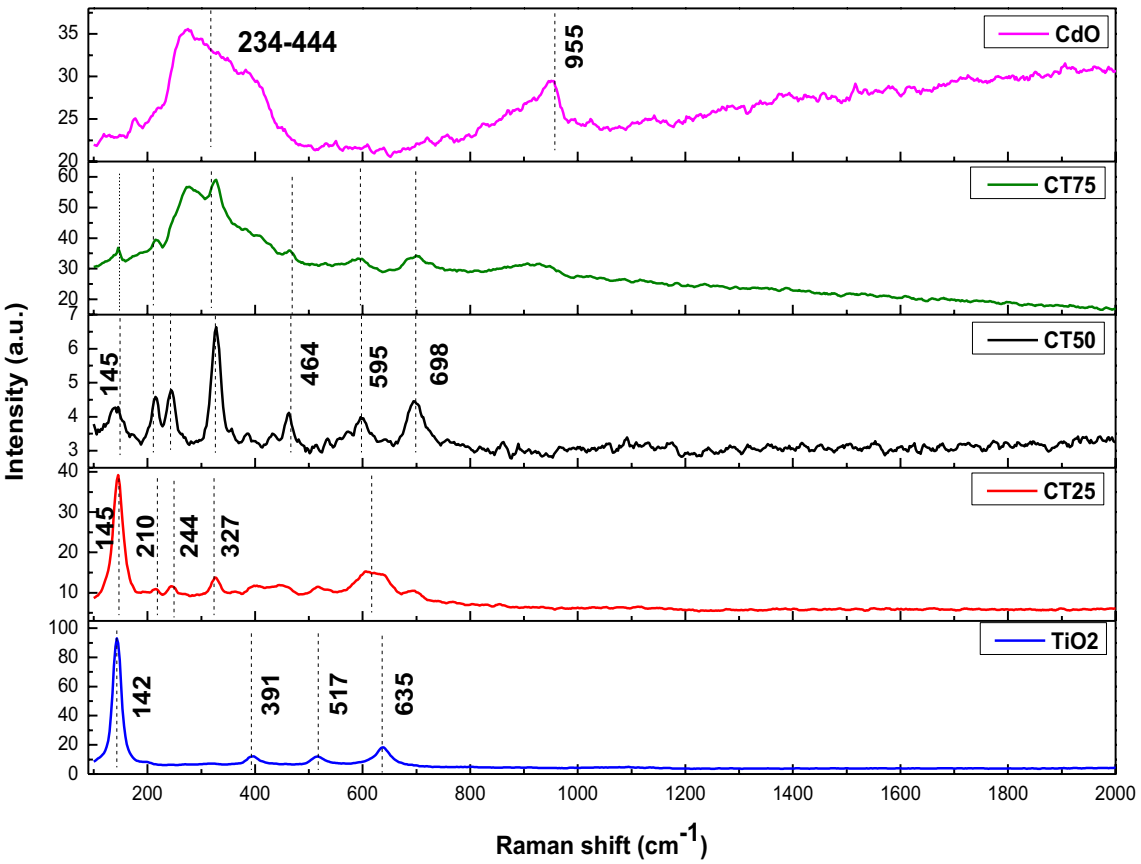

Fig. 2 Raman spectrum of TiO_2, CdO and nanocomposite thin films with different Cd:Ti ratios on glass

in TC75 sample can be related to the crystalline segregation effect and the weak coalescence of nanograins [45].

Figure 2 presents the Raman spectra of pure TiO_2, CdO, and nanocomposite thin films with different ratios of Cd incorporated into TiO_2 matrix. In addition to the typical anatase TiO_2 vibrational peaks that appear in the spectrum of TiO_2, increased incorporation of Cd provokes new vibrational peaks assigned to the rhombohedral $CdTiO_3$ and rutile phase of TiO_2. The Raman bands of the TiO_2 thin films are indicated at 142 cm^{-1} (E_g), 391 cm^{-1}(B_{1g}), 517 cm^{-1} ($A_{1g}+B_{1g}$), and 635 cm^{-1} (E_g) for four allowed modes of pure anatase [46]. As shown in Fig. 2, the Raman peaks have narrow FWHM, which reflect the high structural quality of TiO_2.

The effect of Cd incorporation into TiO_2 matrix becomes obvious by the appearance of new peaks attributed to the two rutile and rhombohedral ilmenite $CdTiO_3$ phases, while bands corresponding to the TiO_2 anatase phase disappear completely. By adding Cd into the TiO_2 matrix for the two lower concentrations, the rutile phase appears in the Raman spectra, according to B_{1g} band at 145 cm^{-1} [47]. On the other side, the characteristic peaks of rhombohedral $CdTiO_3$ are detected at around 210 cm^{-1} (E_{g4}: translation of TiO_6 octahedra with respect to Cd^{2+}), 244 cm^{-1} (A_{g4}: translation of TiO_6 octahedra with respect to Cd^{2+}), 327 cm^{-1} (A_{g3}: O–Cd–O bending mode), 464 cm^{-1} (A_{g2}: O–Cd–O bending mode), 595 cm^{-1} (E_{g1}: Ti–O stretching mode), and 698 cm^{-1} (A_{g1}: Ti–O stretching mode) [41]. Therefore, the rhombohedral (ilmenite) symmetry of $CdTiO_3$ is confirmed in this study by Raman spectra, in accordance with those reported in the literature [36, 48]. In fact, the absence of the characteristic peak at 142 cm^{-1} of anatase and the appearance of new peaks attributed to new phases is an indication of the penetration of Cd^{2+} into the network of TiO_2 [49].

A Raman signal resulting from the crystalline cubic CdO phase was first observed for TC75 samples. The existence of peaks associated to rutile phase of TiO_2 and $CdTiO_3$ showed that the formation of the binary TiO_2–$CdTiO_3$ nanocomposite thin films dominate for TC25 and TC50 films. Altogether, the ternary composite TiO(rutile)–$CdTiO_3$–CdO is confirmed for TC75 films again, indicating the formation of different nanocomposite materials for TC25, TC50, and TC75 samples. These results are in good agreement with those proposed by the X-ray diffraction spectra.

3.2 Morphological analysis

The surface morphology of the films was investigated by Scanning Electron Microscopy (SEM). Figures 3(a, b, c) show the SEM images of pure and nanocomposites (TC25 and TC75) films. It can be seen, for pure TiO_2 (Fig. 3a), that the thin films have a homogenous granular and porous surface. It consists of a uniform distribution of nanograins with no significant differences in size and shape, giving a relatively smooth surface. The surface of the TC25 nanocomposite thin films shows a large number of nanopores and consists of leaf-like particles with irregular shapes and with different sizes (Fig. 3b). Additionally, an image with higher resolution (see figure inset) shows long grains with a rod-like morphology. The surface of the TC75 nanocomposite thin film shows an increase in the number and size of the observed pores with many differences in their shape, Fig. 3c. Moreover, an increase in grain size was observed. This could be due to the increase of the average sizes of the nanocrystallites according to the XRD results.

3.3 Optical analysis

The optical transmittance and reflectivity of pure TiO_2 and CdO and nanocomposite thin films with different Cd:Ti ratios, recorded in the wavelength range of 300–1200 nm, are shown in Fig. 4(a–b). For Ti:Cd ≥ 25%, a high average of transmission was observed in Fig. 4a, higher than 75%. The higher transparencies observed for the TC25 and TC50 samples confirm the proper substitution of Cd into TiO_2 matrix and also reflect the quality of the fabricated materials [50]. After reaching a maximum average for Cd:Ti = 25%, the transparency decreases in particular for Cd:Ti = 75% and pure CdO thin films. The films become increasingly opaque, attributed to the fact that the film surface is rough and consequently the average transmission is respectively low (≤ 40%, in the visible range). The presence of aggregates in SEM images proves the decrease of optical transmittance due to the dispersion effects [51].

This remarkable reduction of the transmission range is accompanied by the reduction of the number of the interference fringes. The presence of these interferences for Ti: Cd ≤ 50% indicates that for TiO_2, TC25, and TC50, the obtained thin films are smooth and micro-structurally homogenous. But for TC75 the increase in nanograin size, as it has been demonstrated from the results of the XRD and SEM images above, leads to an increased surface roughness and therefore to an increase in reflectivity, as Fig. 4b indicates. This in turn leads to a lowering of the average of transmittance and an almost interference disappearance was observed [52]. As a conclusion, the variations in the optical transmittance of the films in the visible region can be explained by the changes in both the crystalline quality and surface roughness of the films due to the different Cd:Ti ratios [53]. On the other hand, the observed reflectivity, in Fig. 4b, is less than 40% for all films.

The transmission spectra showed that Cd incorporation for Cd:Ti ≤ 50% caused a notable blue shift of the transmittance edge.

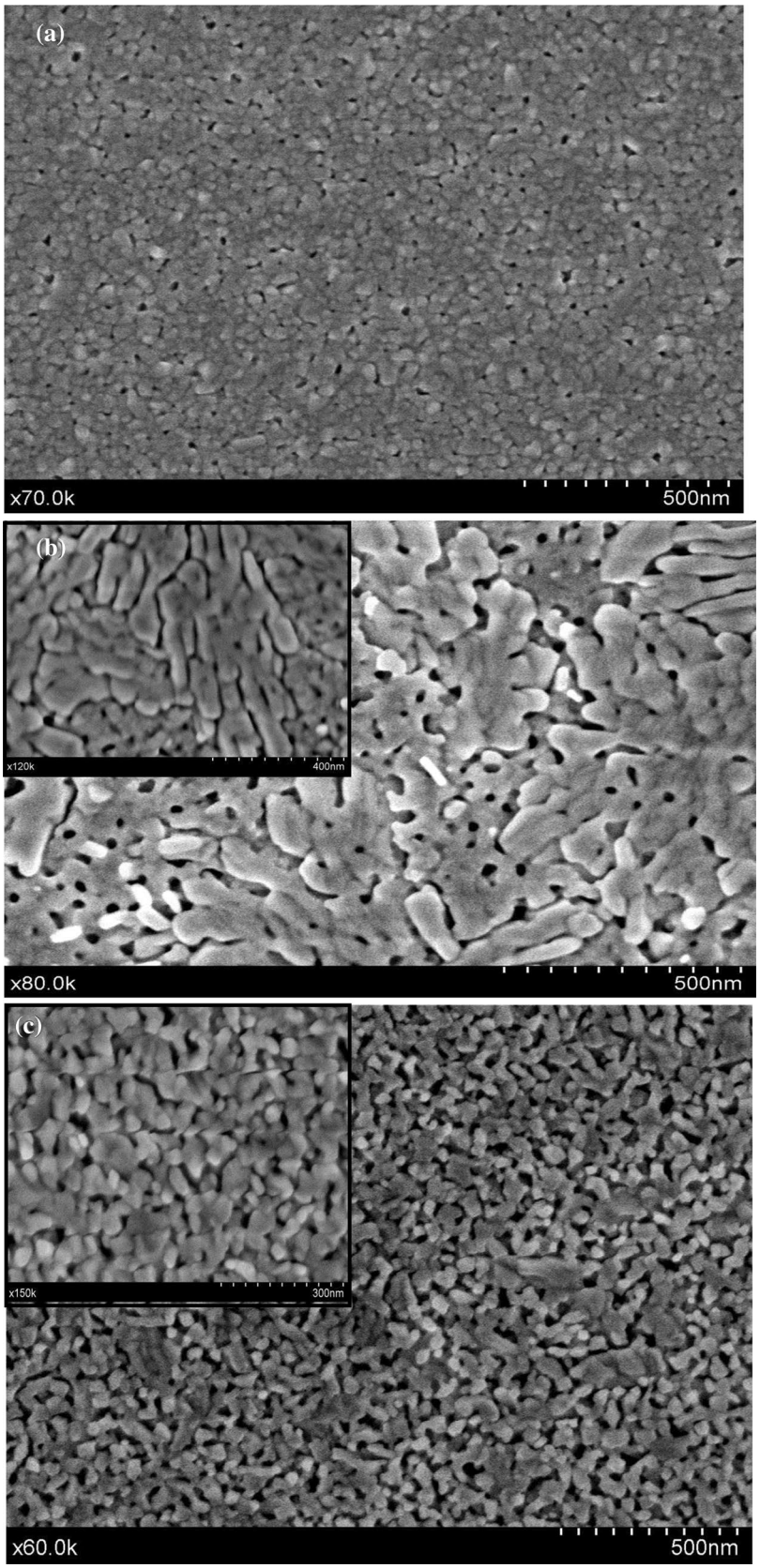

Fig. 3 **a**–**c** SEM images of **a** TiO_2, **b** TC25, and **c** TC75 thin films on glass

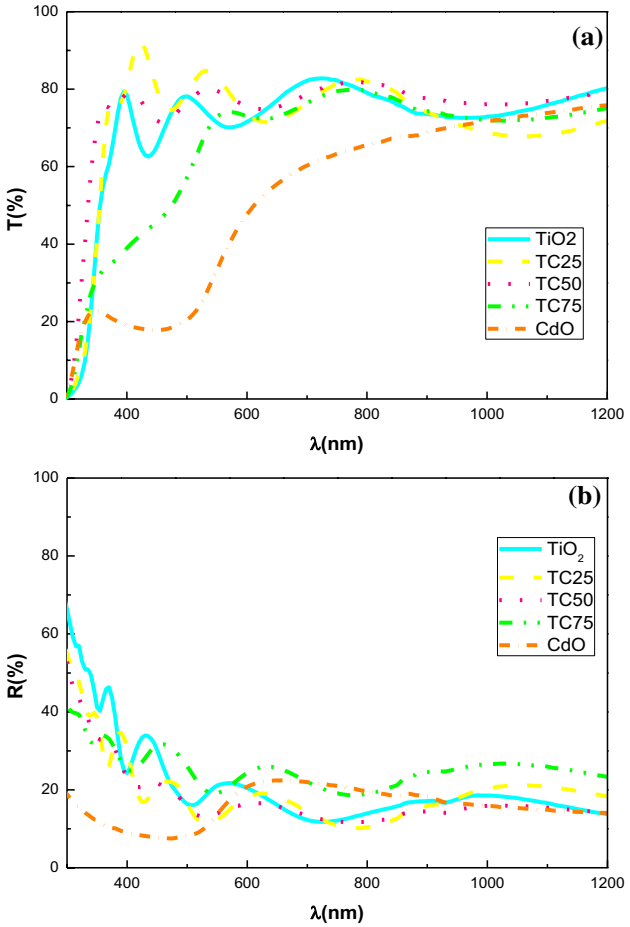

Fig. 4 **a**–**b** Spectral variation of optical **a** transmittance (T) and **b** reflectance (R) spectra of TiO_2, CdO and nanocomposite thin films with different Cd:Ti mass ratio

From the optical spectra, the direct energy bandgap of the deposited thin films was determined using Tauc's relation [10].

$$(\alpha h\nu)^2 = A(h\nu - Eg) \quad (2)$$

where A is a constant, h Planck's constant, ν is frequency, α is the absorption coefficient, and Eg is the bandgap. The bandgap can be obtained by plotting the expression $(\alpha h\nu)^2$ versus hν (Fig. 5a). The bandgap values, as represented in Fig. 5b, are 3.2, 3.38, 3.53, 2.68, and 2.4 eV for TiO_2, TC25, TC50, TC75, and CdO nanocomposites, respectively. The values found for TiO_2 and CdO are in good agreement with those given in the literature [54, 55].

The addition of Cd to TiO_2 leads to a bandgap widening. This initial increase of the optical bandgap of the films (for Cd:Ti = 25 and 50%) may be explained by the fact that the Cd^{2+} ions are substitutionally occupying the Ti^{4+} ionic sites and provide additional free carriers to the film. This causes a shift of the Fermi level into the conduction band and as a result, the effective band gap becomes larger [52, 56], which corresponded to the blue shift of transmission edge as discussed above (Moss–Burstein effect).

On the contrary, a red shift of the transmission edge toward longer wavelengths has been detected for TC75 samples indicating a bandgap of the TC75 nanocomposite narrower than that of TC25 and TC50 ones. Such a shift is due, on one hand, to the structural change, as it was proved by the presence of $CdTiO_3$ phase as well as the phase transformation of TiO_2 (from anatase to rutile), both contributing to reorganization of the structure and to an increased number of impurities. On the other hand, the decrease of Eg can be correlated with grain size [57],as explained above, the grain size is due to aggregates of $CdTiO_3$ and CdO crystalline grains, which are formed separately [53, 58].

4 Conclusion

In the present work, the impact of three (25, 50 and 75%) Cd:Ti ratios on the structural, morphological, compositional, and optical properties of different binary TiO_2–$CdTiO_3$ and ternary composite TiO_2 (rutile)–$CdTiO_3$–CdO nanocomposite thin films, grown by the spin coating technique, were studied and discussed. From XRD analysis, it was found that the structural properties of pure TiO_2 were clearly modified by increasing the Cd:Ti ratios. This was attributed to the Cd^{2+} ions substitution into the TiO_2 lattice in all nanocomposite thin films that led to a phase transformation (anatase to rutile), accompanied by formation of the spinal phase $CdTiO_3$ (ilmenite rhombohedral) at $T = 450$ °C annealing temperature. The Raman analysis revealed the appearance of the rutile phase of TiO_2 and the spinal $CdTiO_3$. Raman spectra also proved this phase transformation by varying the Cd:Ti ratio in accordance with the XRD results. The SEM images showed that the surface grains of the TiO_2–CdO nanocomposite thin films were strongly affected in shape and size with the increase of the Cd:Ti ratio. Optical spectra revealed high optical transmission of the films with values that were also affected by the Cd:Ti ratios. Film energy bandgaps have been estimated from the optical spectra, resulting to an increased Eg value for the TC25 and TC50 nanocomposite films, while a decreased value for the TC75 one, in respect to the pure TiO_2 thin film. This behavior could be interpreted with the aid of the structural and morphological results. It has been shown therefore that the

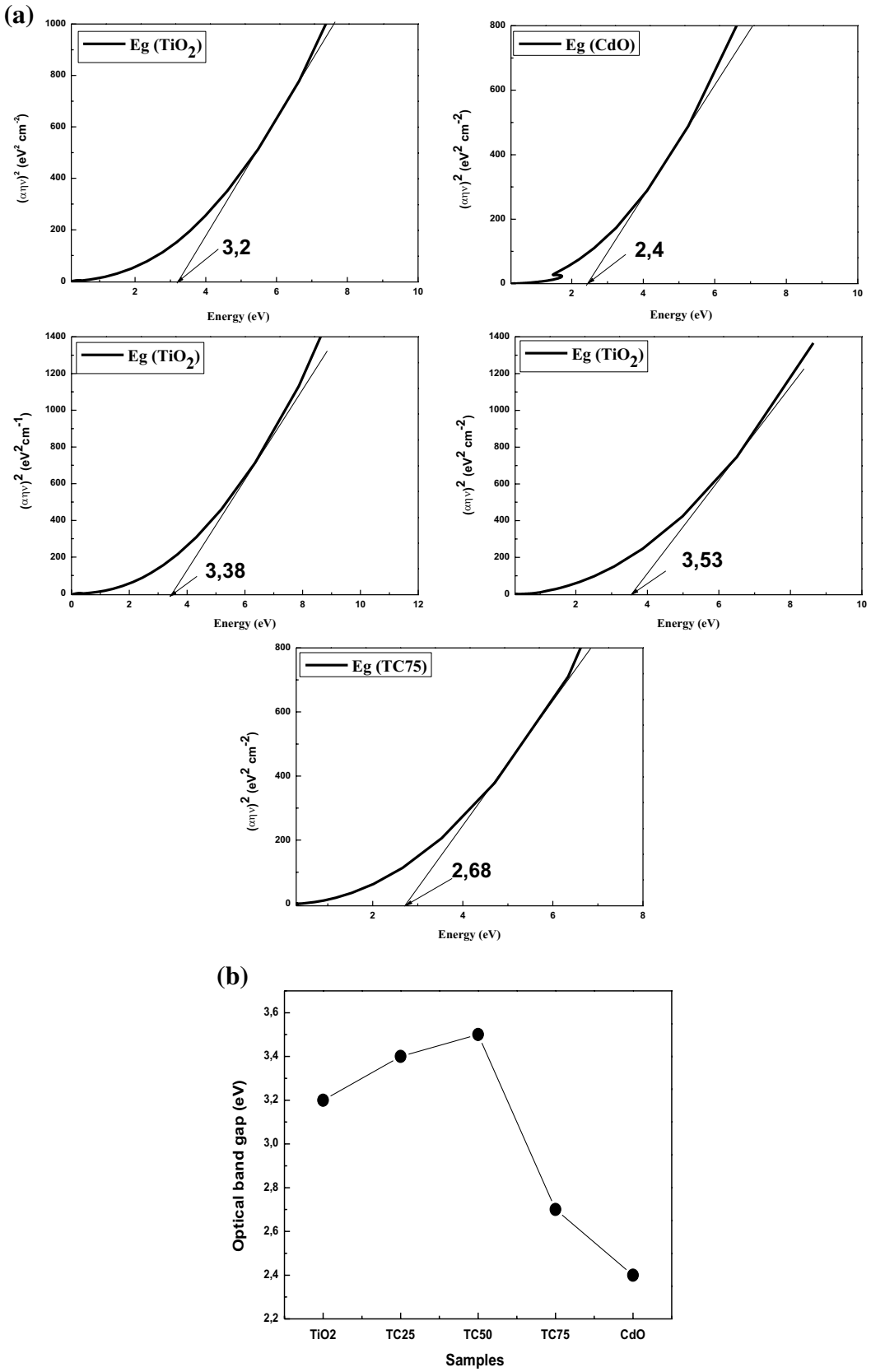

Fig. 5 **a** Tauc plots of TiO_2, CdO and nanocomposite thin film with different Cd:Ti ratios on glass. **b** Optical band gap variation of TiO_2, CdO and nanocomposite thin films with different Cd:Ti ratios on glass

applied method is suitable to grow samples with specific physical properties that can fulfill demands of various electronic device applications.

Acknowledgments Part of this work has been performed in the Nanotechnology on Surfaces Laboratory, Institute of Materials Science of Seville (CSIC-Univ. Seville), Seville ES-41092, Spain and financed by the Tunisian Ministry of Higher Education and Scientific Research.

References

1. S. Zhang, F. Yongqing, D. Hejun, Y. Liu, T. Chen, Adv. Mater. Micro. Nano. Syst. **1721**(1), 3836 (2004)
2. S. Zhang, D. Sun, Y. Fu, H. Du, Surf. Coat. Technol. **167**(2–3), 113–119 (2003)
3. J. Musil, Surf. Coat. Technol. **125**(1–3), 322–330 (2000)
4. S. Veprek, S. Reiprich, Thin Solid Films **268**(1–2), 64–71 (1995)
5. L. Maya, W.R. Allen, Gold nanocomposites. J. Vac. Sci. Technol. B **13**(2), 361–365 (1995)
6. F. Mazaleyrat, L.K. Varga, J. Magn. Magn. Mater. **215–216**, 253–259 (2000)
7. P.A. Radi, A.G. Brito-Madurro, J.M. Madurro, N.O. Dantas, Br. J. Phys. **36**(2a), 412–414 (2006)
8. B. Cantor, C.M. Allen, R. Dunin-Burkowski, M.H. Green, J.L. Hutchinson, K.A.Q. O'Reilly, A.K. Petford-Long, P. Schumacher, J. Sloan, P.J. Warren, Scripta Mater. **44**, 2055–2059 (2001)
9. C.V. Reddy, B. Babu, J. Shim, J. Phys. Chem. Solids **112**, 20–28 (2018)
10. H.A. Azimi-Fouladi, S.A. Hassenzadeh-Tabrizi, A. Saffar-Teluri, Ceram. Int. **44**(4), 4292–4297 (2018)
11. R. Saravanan, H. Shankar, T. Prakash, V. Narayanan, A. Stephen, Mater. Chem. Phys. **125**(1–2), 277–280 (2011)
12. Ü.Ö.A. Arier, Optik **127**(16), 6439–6445 (2016)
13. P. Margan, M. Haghighi, J. Sol-Gel Sci. Technol. **81**(2), 556–569 (2017)
14. K. Karthik, S. Dhanuskodi, C. Gobinath, S. Prabukumar, S. Sivaramakrishnan, J. Phys. Chem. Solids. **112**, 106–118 (2018)
15. H. Taniguchi, H. Moriwake, T. Yagi, M. Itoh, Adv. Ferroelectr. **13**, 279 (2013)
16. M.E. Guzhva, V.V. Lemanov, P.A. Markovin, Phys. Solid State **43**(11), 2146–2153 (2011)
17. V. Gupta, K.K. Bamzai, P.N. Kotru, B.M. Wanklyn, Mater. Sci. Eng. B **130**(1–3), 163–172 (2006)
18. D. Ponnusamy, A.K. Prasad, S. Madanagurusamy, Mikrochim. Acta **183**(1), 311–317 (2016)
19. Z.N. Abdul-Ameer, I.R. Agool, World Sci News **23**, 35–45 (2015)
20. F. Hanini, A. Bouabellou, Y. Bouachiba, F. Kermiche, A. Taabouche, K. Boukheddaden, Afrique Sci. **10**(1), 10–20 (2014)
21. A. Stoyonova, H. Hitkova, A. Bachvarova Nedelcheva, R. Iordanova, N. Ivanova, M. Sredkova, J. Chem. Technol. Metall. **48**(2), 154–161 (2013)
22. A. Shalaby, A. Bachvarova Nedelcheva, R. Iordanova, Y. Dimitriev, A. Stoyanova, H. Hitkova, N. Ivanova, M. Sredkova, J. Optoelectron. Adv. Mater. **17**(1–2), 248–256 (2015)
23. R. Bahloul, S. Sayouri, K. Limame, M.M. Yahyaoui, B. Jaber, L. Laonab, J. Ceram. Process. Res. **18**, 1–7 (2017)
24. S.B. Kokane, S.D. Sartale, K.G. Girijia, I. Jagannath, R. Sasikala, Int. J. Hydrogen Energy **40**(39), 13431–13442 (2015)
25. F.A. Harnández-Garia, G. Torres-Delgado, R. Castanedo-Pérez, O. Zelaya-Angel, J. Photochem. Photobiol. A **310**, 52–59 (2015)
26. H.M. Ghuson, M.S. Ahmed, K. Dunia, A.A. Kadhim, Eng. Technol. J. **33**(5), 918–931 (2015)
27. S.A. Mayén-Harnandez, J. Santos-Cruzy, G. Torres-Delgado, R. Castanedo-Pérez, J. Marquez-Marin, J.C. Mendoza-Alverez, O. Zelaya-Angel, Surf. Coat. Technol. **200**(11), 3567–3572 (2006)
28. Z.H. Cui, F. Wu, H. Jiang, Phys. Chem. Chem. Phys. **18**, 29914–29922 (2016)
29. T. Mazza, E. Barborini, P. Piseri, P. Milani, D. Cattaneo, A. Li Bassi, C.E. Bottani, C. Ducati, Phys. Rev. B **75**(4–15), 045416 (2007)
30. D.A.H. Hanaor, C.C. Sorrell, J. Mater. Sci. **46**(4), 855–874 (2011)
31. K. Sahbeni, I. Sta, M. Jlassi, M. Kandyla, M. Hajji, M. Kompitsas, W. Dimassi, J. Phys. Chem. Biophys. **7**(3), 257 (2017)
32. T. Mitsuhashi, O.J. Kleppa, J. Am. Ceram. Soc. **62**(7–8), 356–357 (1979)
33. D. Barsani, P.P. Lottici, M. Canali, A. Montenero, J. Sol–Gel Sci. Technol. **8**, 337–342 (1997)
34. C. Karunakaran, A. Vijayabalan, Mater. Sci. Semicond. Process. **16**(6), 1992–1996 (2013)
35. P. Dhivya, A.K. Prasad, M. Sridharan, Sens. Actuators B. **222**, 987–993 (2016)
36. M.S. Hassan, T. Amna, M.S. Khil, Ceram. Int. **40**(1), 423–427 (2014)
37. F. Dachiller, P.Y. Simons, R. Roy, Am. Miner. **53**(11–12), 1929–1939 (1968)
38. R.D. Shannon, J.A. Pask, J. Am. Ceram. Soc. **48**(8), 391–398 (1965)
39. Z.M. Wang, G. Yang, P. Biswas, W. Bresser, P. Boolchand, Powder Technol. **114**(1–3), 197–204 (2001)
40. Y.C. Zhang, G.L. Wang, X.Y. Hu, W.D. Zhou, J. Cryst. Growth. **285**(4), 600–605 (2005)
41. M. Kharkwal, S. Uma, R. Nagarajan, Indian. J. Chem. **51**(11), 1538–1544 (2012)
42. J.G. Huang, X.T. Guo, B. Wang, L.Y. Li, M.X. Zhao, L.L. Dong, X.J. Liu, Y.T. Huang, J. Spectrosc. **8**, 681850 (2015)
43. S. Yun, S. Lim, J. Colloid Interface Sci. **360**(2), 430–439 (2011)
44. M. Chaari, A. Matoussi, Mater. Sci. Eng. B **178**(17), 1130–1139 (2013)
45. M.C. Mathpal, A.K. Tripathi, M.K. Singh, S.P. Gairola, S.N. Pandey, A. Agarwal, Chem. Phys. Lett. **555**, 182–186 (2013)
46. N. Khatun, P.R. Anita, D. Bhattacharya, S.N. Jha, S. Biring, S. Sen, Ceram. Int. **43**(16), 14128–14134 (2017)
47. S.A. Mayén-Harnandez, G. Torres-Delgado, R. Castanedo-Pérez, J.G. Mendoza-Alvarez, O. Zelaya-Angel, Mater. Chem. Phys. **115**(2–3), 530–535 (2009)
48. C.L. Luu, Q.T. Nguyen, S.T. Ho, T. Nguyen, Adv. Nat. Sci. **4**(3), 035003–035015 (2013)
49. P. Sakthivel, S. Muthukumaran, M. Ashokkumar, J. Mater. Sci. **26**(3), 1533–1542 (2015)
50. I.E. Paulauskas, D.R. Modeshia, T.T. Ali, E. El-Mossalamy, A.Y. Obaib, S.N. Bsahel, A.A. Al-Ghamdi, F.K. Sartain, Platinum Met. Rev. **57**(1), 32–43 (2013)
51. S.M.H. Al-Jawad, A.A. Taha, M.M. Salim, Optik **142**, 42–53 (2017)
52. T. Srinivasulu, K. Saritha, K.T. Ramakrishna Reddy, Mod. Elect. Mat. **3**(2), 76–85 (2017)
53. M.E. de Anda Reyes, G. Torres Delgado, R. Castanedo Perez, J. Màrquez Marin, O. Zelaya Angel, J. Photochem. Photobiol. A **228**(1), 22–27 (2012)
54. I. Sta, M. Jlassi, M. Hajji, M.F. Boujmil, R. Jerbi, M. Kandyla, M. Kompitsas, H. Ezzaouia, J. Sol-Gel Sci. Technol. **72**, 421–427 (2014)
55. I. BenMiled, M. Jlassi, I. Sta, M. Dhaouadi, M. Hajji, G. Mousdis, M. Kompitsas, H. Ezzaouia, J. Sol-Gel Sci. Technol. **83**(2), 259–267 (2017)
56. J.C. Yu, W. Ho, Z. Jiang, L. Zhang, Chem. Mater. **14**(9), 3808–3816 (2002)
57. A. Boutlala, M. Mahtili, A. Bouaballou, Mater. Sci. Eng. **108**, 012048 (2016)

58. P. Banerjee, W.J. Lee, K.R. Bae, S.B. Lee, G.W. Rubloff, J. Appl. Phys. **108**, 043504 (2010)